Available online at www.sciencedirect.com

ScienceDirect

journal homepage: www.elsevier.com/locate/he

Microfluidic hydrogen storage capacity and residual trapping during cyclic injections: Implications for underground storage

Maksim Lysyy[*], *Na Liu*, *Celine M. Solstad*, *Martin A. Fernø*, *Geir Ersland*

Department of Physics and Technology, University of Bergen, Allegaten 55, 5007 Bergen, Norway

HIGHLIGHTS

- Microfluidics for examination of cyclic hydrogen injections.
- Microscopic hydrogen storage capacities up to 60% of the pore space.
- Reproducible residual hydrogen saturation between the injection cycles.
- Efficient reconnection of residually trapped hydrogen in the next drainage cycle.

GRAPHICAL ABSTRACT

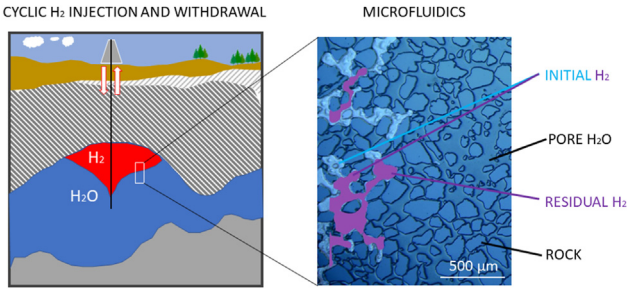

ARTICLE INFO

Article history:
Received 31 January 2023
Received in revised form
19 April 2023
Accepted 22 April 2023
Available online 11 May 2023

Keywords:
Microfluidics
Underground hydrogen storage
Cyclic flow
Storage capacity
Residual trapping

ABSTRACT

Long-term and large-scale H_2 storage is vital for a sustainable H_2 economy. Research in underground H_2 storage (UHS) in porous media is emerging, but the understanding of H_2 reconnection and recovery mechanisms under cyclic loading is not yet adequate. This paper reports a qualitative and quantitative investigation of H_2 reconnection and recovery mechanisms in repeated injection-withdrawal cycles. Here we use microfluidics to experimentally investigate up to 5 cycles of H_2 injection and withdrawal under a range of injection rates at shallow reservoir storage conditions. We find that H_2 storage capacities increase with increasing injection rate and range between ~10% and 60%. The residual H_2 saturation is in the same range between cycles (30–40%), but its distribution in the pore space visually appears to be hysteretic. In most cases, the residually trapped H_2 reconnects in the subsequent injection cycle, predominantly in proximity to the large pore clusters. Our results provide valuable experimental data to advance the understanding of multiple H_2 injection cycles in UHS schemes.

* *Corresponding author*. University of Bergen, Department of Physics and Technology, Allegaten 555007 Bergen Norway.
E-mail address: maksim.lysyy@uib.no (M. Lysyy).

https://doi.org/10.1016/j.ijhydene.2023.04.253

Introduction

Hydrogen (H_2) is an emission-free energy carrier and its wider use can contribute to climate change mitigation by decreasing the share of fossil fuels in the global energy mix. Full-scale industrial implementation in a global H_2 economy will require numerous storage sites and solutions [1]. Future H_2 storage demand in Europe is predicted to range between 63 and 180 billion standard m^3 in 2050, assuming H_2 total demand of 780–2251 TWh [2] and 24% storage capacity [3]. Underground H_2 storage (UHS) in depleted hydrocarbon fields and aquifers has been proposed as a reliable and safe storage technology due to the presence of an impermeable seal and large pore space [4,5]. The technicalities are similar to natural gas storage (UGS), where cushion gas remains in reservoir to maintain the target pressure and working gas is injected at peak supply (summer) and withdrawn at peak demand (winter). However, H_2 is a low density and low viscosity gas with high diffusivity and biogeochemical reactivity and therefore its behavior in porous media will differ from that of other gases. The experience with UHS in porous media is limited to: 1) two pilot tests in depleted gas fields [6,7] and 2) town gas storage in aquifers [8,9].

Scientific challenges relevant for the UHS arise from H2 physical properties as well as reactions with rock minerals and microorganisms, potentially reducing the storage efficiency [5,10]. H_2 injections are prone to unstable displacement and gravity override due to low viscosity and density. Moreover, a certain amount of H_2 may be permanently lost during storage operation by various physical, chemical and operating loss mechanisms [4]. Reservoir simulation and wettability studies are currently dominating the research literature in the field of UHS flow physics. Storage capacities and recovery factors have been estimated using conceptual reservoir models with extrapolated input parameters not specifically measured for H_2 [11,12].

Contact angle measurements indicated that H_2 is a non-wetting fluid on pure quartz surfaces and sandstones but shifts to intermediate-wet state in the presence of organic acids [13–16]. No clear difference in contact angles was reported between H_2, CH_4, H_2–CH_4 mixtures and N_2 using a captive-bubble method in sandstones and a borosilicate micromodel at pressures between 10 and 100 bar [17,18]. On the other hand, CO_2 was found to be more wetting, i.e. higher contact angles, compared to H_2 [13,16]. Note that the contact angle differences between various gases are expected to become more pronounced at pressures above 100 bar due to the increasing gas density differences, shown for basaltic rocks [19]. Moreover, rock-gas interfacial tension calculations indicated significant differences between H_2, CH_4 and CO_2 [20]. There are also discrepancies regarding the influence of pressure, temperature and salinity on H_2 wettability. H_2 contact angles increased with increasing pressure and temperature when using the tilted plate method [13,16], whereas no meaningful effect of pressure, temperature and salinity was reported using the captive bubble technique under a range of 7–207 bar, 20–50 °C and 1000–50000 ppm NaCl brine [14,15,17].

Neither reservoir simulations nor wettability studies can adequately describe pore scale influencing factors on UHS such as interactions between H_2, reservoir rock and its native fluid as well as trapping mechanisms [21]. Residual trapping is recognized as one of the major H_2 loss mechanisms [4,22], which is expected to decrease with decreasing capillary forces and increasing H_2 wetting [23]. The UHS involves multiple cycles of H_2 injection (drainage) and withdrawal (imbibition), and residual trapping occurs during imbibition where water is available and mobile in the reservoir, e.g. in the H_2–H_2O transition zones. The residually trapped H_2 ganglia may reconnect during drainage due to hysteresis. Hysteresis was evident from relative permeability measurements [24,25] and microfluidic-based contact angle measurements [26], but it remains unaddressed for several injection-withdrawal cycles.

A few laboratory investigations of H_2 residual trapping used in-situ visualization of a single drainage-imbibition cycle in different sandstones. The initial and residual H_2 saturations in the pore space (values between 0 and 1) were measured to be 0.65 and 0.41, respectively [27]. H_2 recovery decreased from 43.1% when flooded with non-H_2-equilibrated brine to 31.6% for H_2-equilibrated brine [28]. The initial H_2 saturation was ~6 times lower compared to N_2 using the same injection rate [29]. No clear pressure impact on the initial H_2 saturation was evident, contrary to H_2 residual trapping which increased with increasing pressure and decreasing injection rate [30].

H_2 cyclic injections were only performed for two drainage-imbibition cycles and resulted in similar initial and residual H_2 saturations: 0.48 and 0.07, respectively [30]. In contrast, cyclic injections have been extensively investigated for CO_2 storage, where some studies indicated an increased residual trapping over the injection cycles [31–33], contradicting a classic trapping theory [34]. More systematic studies with the increased number of injection cycles are required to find out whether the multiple injection cycles can potentially result in hysteresis and increase H_2 residual trapping.

Microfluidics is a valuable tool for direct observations of pore space to corroborate core scale measurements. Small pore volumes are beneficial for the sake of time and safety when working with highly flammable H_2 gas at elevated pressures. In this work, we qualitatively describe hysteretic H_2 trapping and reconnection mechanisms during cyclic injections in a silicon-wafer micromodel with pore patterns resembling a natural sandstone. Up to 4–5 drainage-imbibition cycles were run under a wide range of injection rates at 40 bar and ambient temperature, representing the storage conditions of a shallow aquifer or a gas-water transition zone in a depleted gas field. An in-house MATLAB code was developed to quantify microscopic H_2 storage capacity, residual trapping and recovery factors. Our results add new experimental data, enhancing the understating of hysteretic H_2 behavior during multiple injection cycles.

Materials and methods

Porous material

We used a silicon micromodel capable of withstanding pressure up to 150 bar (Fig. 1). The irregular sandstone-based pore patterns (pure quartz) were etched and repeated 36 (4 × 9) times on the silicon wafer using deep reactive ioning etching

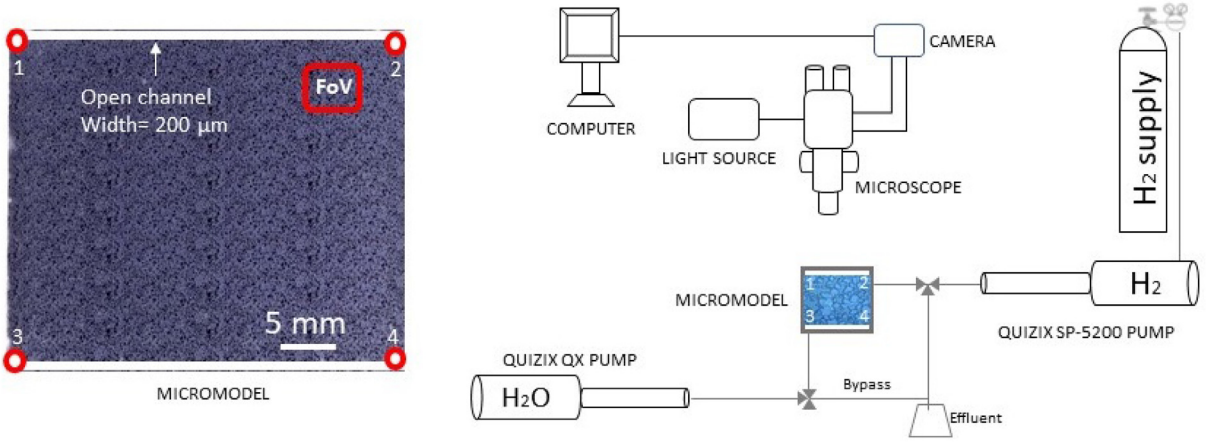

Fig. 1 – Left: Micromodel with irregular pore patterns replicating natural sandstone. The micromodel was built with four ports (1–4) and two open channels (from the ports 1 to 2 and from 3 to 4). The field of view (FoV) refers to the micromodel area observed by the microscope (not to scale). Right: Experimental setup consisting of the micromodel, two pumps for H_2 and H_2O injections and pressure control as well as the microscope equipped with the light source and the camera. H_2 and H_2O were injected diagonally from the opposite ports, i.e. from ports 2 and 3, respectively.

(DRIE) with an etching depth of 30 μm. The DRIE technique ensured a correct reproduction of morphological and topological features, preserving the sharp grain walls with a surface roughness of 100 nm and high aspect ratio and coordination number, which ensured a correct magnitude of the capillary forces. The micromodel top (transparent borosilicate glass) and bottom (silicon) surfaces were anodically bonded and produced with strongly hydrophilic surfaces, with measured H_2 contact angles ranging between 19° and 60°. The micromodel surfaces were not aged in organic acids, making them more hydrophilic than natural reservoirs [13,16]. The micromodel has two open channels (100% void space), connected from ports 1 to 2 and from 3 to 4. The pore network has a length of 27 mm and a width of 21.4 mm, with a total porosity of 61% (Table 1). The micromodel studied region is defined as the field of view (FoV) and represents approximately 1% of the entire area micromodel. A more detailed description of the micromodel construction procedure and its properties can be found elsewhere [35,36].

Experimental setup and procedures

The micromodel was assembled in the PEEK holder with four outlet ports connected to the 1/16″ PEEK tubing, where two tubes from the diagonally located ports (2 and 3) were connected to two Quizix pumps through 1/16" stainless-steel tubing (Fig. 1). Quizix QX pump was filled with filtered deionized H_2O, whereas H_2 was accommodated by Quizix SP-5200 pump (cylinder C5000-10K-SS-AT). A microscope (Nikon SMZ1500) connected to a camera (Nikon D7100) and computer enabled us to directly observe the micromodel FoV, which was illuminated by a light source with spot lighting (Photonic LED F1 Cold light 5500K).

Table 1 – Micromodel properties.

	Micromodel	Micromodel FoV
Length [mm]	27	3.5
Width [mm]	21.4	1.96
Depth [μm]	30	
Pore volume [μL]	11	0.09
Porosity [frac.]	0.61	0.44
Permeability [D]	2.97	
Pore throat length [μm]	10–300	

Two different groups of experiments were performed at pore pressure of 40 bar and ambient temperature (20 ± 1 °C): 1) Single-cycle of H_2 injection and withdrawal, i.e. primary drainage and imbibition only (experiments A1-A4) and 2) multiple cycles of H_2 injection and withdrawal (experiments B1–B4). An overview of experiments and key results are shown in Table 3. In the experiments A1-A4, the H_2O pump was used for H_2O withdrawal (drainage) and injection (imbibition), whereas the constant pressure in the micromodel was maintained by the H_2 pump. In total, single-cycle injection-withdrawal experiments were performed four times at different injection rates in the range of 0.1–50 mL/h.

In experiments B1–B4, the pump operation modes were different. During drainage, the H_2O pump was set to constant pressure and H_2 was injected from the H_2 pump at constant flow rate. After drainage, the tubing connection from the H_2O pump to the micromodel was cleaned with H_2O via the by-pass tubing to remove the remaining H_2, preventing the H_2–H_2O slug flow in the micromodel. During imbibition, both pumps were operated at constant flow rates where H_2O was injected in the micromodel while the piston in the H_2 pump retracted. Imbibition was terminated after the establishment of the residually trapped H_2 ganglia. Then the system was ready for a new drainage-imbibition cycle, which was repeated three-four times. Prior to a new cycle, H_2 was injected to the bypass line to remove the remaining H_2O. In total, four cyclic experiments were run at various injection rates in the range of 1–10 mL/h.

Dimensionless numbers describe the interplay between various forces acting on two-phase flow. In this work, the capillary number (the ratio of viscous to capillary forces) is defined as $N_{Ca} = U \bullet \mu/\sigma$, where U is the injection velocity [m/s], μ is the invading fluid viscosity [$\mu_{H2} = 8.8 \times 10^{-6}$ Pa s and

Table 2 – Flow conditions: Injection rate (Q) and injection velocity (U); and dimensionless numbers: Capillary (N_{Ca}), Reynolds (Re), Peclet (Pe), and Bond numbers (Bo).

Q [mL/h]	U [m/day]	N_{Ca}		Re		Pe	Bo
		Drainage	Imbibition	Drainage	Imbibition		
0.1	4.9	6.8×10^{-9}	7.7×10^{-7}	0.002	0.006	1.6	0.0017
1	48.6	6.8×10^{-8}	7.7×10^{-6}	0.02	0.06	15.9	
2.5	121.4	1.7×10^{-7}	1.9×10^{-5}	0.06	0.16	39.7	
5	242.9	3.4×10^{-7}	3.8×10^{-5}	0.12	0.32	79.3	
10	485.7	6.8×10^{-7}	7.7×10^{-5}	0.23	0.63	158.6	
50	2428.7	3.4×10^{-6}	3.4×10^{-4}	1.16	3.17	793.2	

Table 3 – Initial (S_{gi}) and residual (S_{gr}) H_2 saturations and recovery factors, defined as $(S_{gi} - S_{gr})/S_{gi}$, during single-cycle (A1-A4) and multiple-cycles (B1–B4) injections.

Exp ID	Q [mL/h]	Cycle number	S_{gi} [fraction]	S_{gr} [fraction]	Recovery factor [fraction]
A1	0.1	1	0.09	0.04	0.53
A2	1	1	0.18	0.05	0.71
A3	10	1	0.61	0.33	0.45
A4	50	1	0.47	0.30	0.38
B1	1	1	0.14	0.03	0.44
		2	0.09	0.04	0.49
		3	0.13	0.07	0.48
		4	0.06	0.08	N/A
B2	2.5	1	0.36	0.35	0.02
		2	0.45	0.40	0.10
		3	0.50	0.42	0.16
		4	0.38	0.33	0.17
		5	0.73	0.48	0.34
B3	5	1	0.42	0.32	0.23
		2	0.60	0.31	0.48
		3	0.67	0.28	0.59
		4	0.53	0.32	0.40
		5	0.60	0.34	0.42
B4	10	1	0.50	0.29	0.42
		2	0.56	0.31	0.45
		3	0.42	0.29	0.32
		4	0.62	0.27	0.57
		5	0.58	0.28	0.51

$\mu_{H2O} = 1.0 \times 10^{-3}$ Pa s [37]], and σ is the H_2–H_2O interfacial tension [= 0.073 N/m [38]]. The injection velocity was calculated as follows: $U = Q/(L{\cdot}d{\cdot}\phi)$, where Q is the injection rate [m^3/s], ϕ is the micromodel porosity [faction], and L and d are the micromodel length and depth [m], respectively. The Reynolds number (the ratio of inertial to viscous forces) is defined as $Re = \rho{\cdot}U{\cdot}D_{50}/\mu$, where ρ is the invading fluid density [$\rho_{H2} = 3.2$ kg/m^3 and $\rho_{H2O} = 1000$ kg/m^3] and D_{50} = median grain diameter [= 1.1×10^{-4} m] – an approximation of the characteristic length scale [39]. The Peclet number correlates convection and diffusion transport and is defined as $Pe = U{\cdot}D_{50}/D$, where D is the H_2 diffusion coefficient through water equal to 4×10^{-9} m^2/s [40]. The Bond number (the ratio of gravitational to surface tension forces) is defined as $Bo = \Delta\rho{\cdot}g{\cdot}(D_{50})^2/\sigma$, where $\Delta\rho$ is the density difference between H_2 and H_2O, and g is the acceleration due to gravity. The range of various dimensionless numbers (Table 2) was estimated at experimental conditions and indicated that the H_2–H_2O flow occurred under the laminar flow regime, with the dominance of convection and surface tension (i.e., capillary forces) over diffusion and gravity. The interplay between viscous and capillary forces was non-trivial where both forces could compete because the experimental N_{Ca}-range belongs to the transition zone in the Log (N_{Ca})-flow diagram [26,41].

Image analysis

The raw images were processed and analyzed to calculate the FoV porosity and H_2 saturation using a combination of an open-source ImageJ software and in-house MATLAB code. The color gradients due to a spotlight required the image pre-processing with manual segmentation of the grains. The FoV porosity was therefore calculated for each image using color thresholding in ImageJ before further analysis in MATLAB. The H_2 saturations were calculated based on the in-house MATLAB code that used the background subtraction algorithm, with a background image of 100% H_2O-saturated FoV. The average relative uncertainty of H_2 saturation was estimated to be 9% and was related to the noise threshold, caused by inclusion of the H_2O droplets and small grains in the H_2 saturation. By adjusting a threshold value of several sequential images with equal quasi-steady-state H_2 saturation, the relative uncertainty was calculated as standard deviation.

Results and discussion

Displacement, trapping and re-connection mechanisms

Primary drainage injections at low rates (≤1 mL/h) resulted in the low H_2 saturation in the FoV ($S_g < 0.20$) due to high capillary entry pressures (Fig. 2, Table 3). At high injection rates (≥10 mL/h) the H_2 saturation increased by ~2–3 times and both connected and disconnected H_2 established due to Roof snap-off [42]. H_2 displacement and trapping during imbibition was governed by I1 imbibition and I2 imbibition mechanisms, respectively [43]. H_2 was displaced from several pores to a single pore (I1 imbibition), where H_2 was disconnected at the pore wall and residually trapped (I2 imbibition). Distribution of the residually trapped H_2 after imbibition (red + purple in Fig. 2) depended on the initial H_2 distribution after drainage (blue + purple in Fig. 2). In most cases, the residually trapped H_2 remained in the same pores (purple in Fig. 2c and d), but displacement to the neighboring pores was also observed (red in Fig. 2c and d). The observed displacement and trapping mechanisms corroborated our previous study in the same micromodel at 5 bar [26], suggesting that displacement

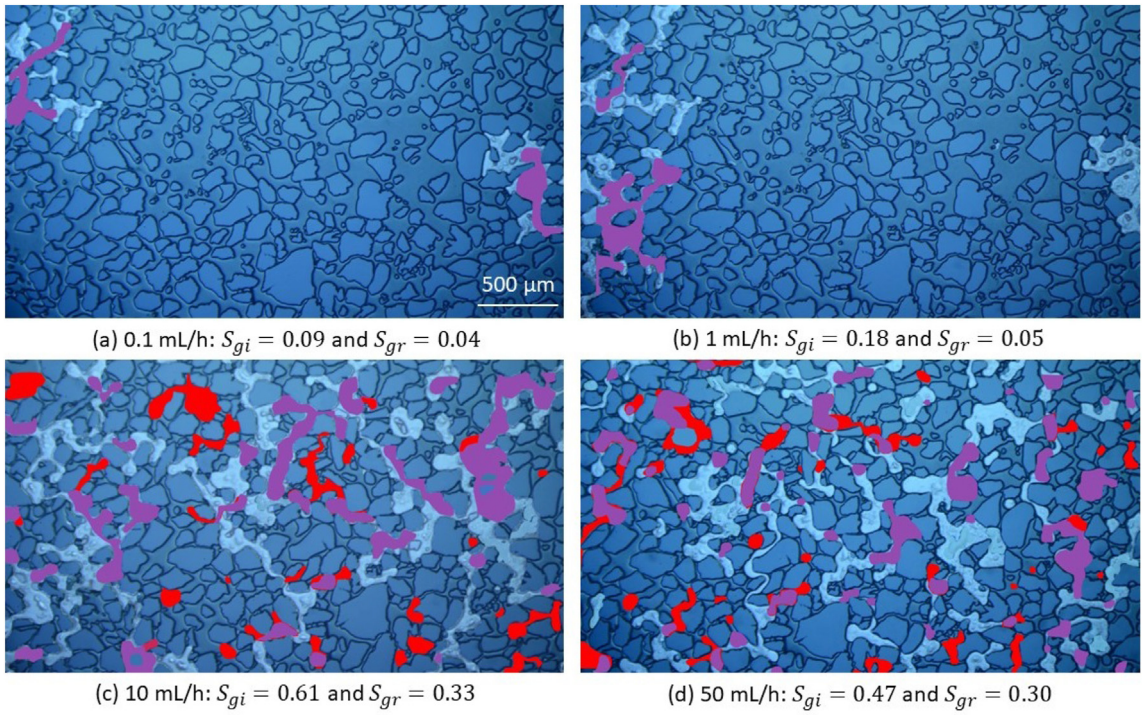

Fig. 2 – Combined images of H_2 saturation after primary drainage, S_{gi} (blue + purple), and after imbibition, S_{gr} (red + purple). Purple color highlights the intersection area of the H_2-filed pore space after drainage and after imbibition. The S_{gi} depended on the injection rate, with higher rates (≥10 mL/h) yielding higher S_{gi}. In most cases, the S_{gr} resided in the same pores as the S_{gi} (purple) but could also redistribute to the neighboring pores indicated with red color. (For interpretation of the references to color in this figure legend, the reader is referred to the Web version of this article.)

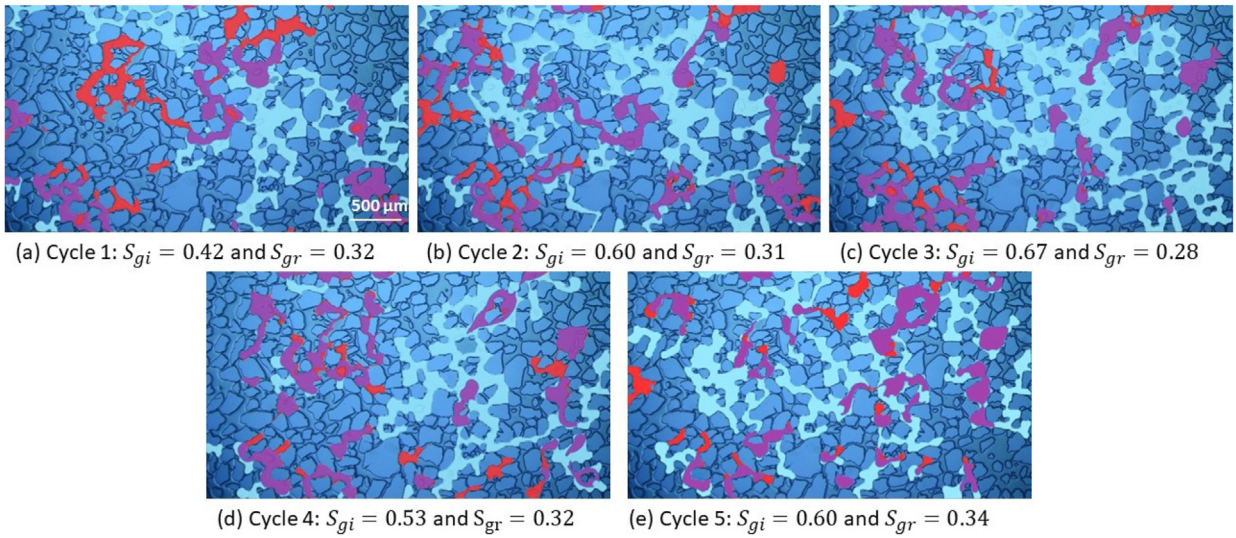

Fig. 3 – Cyclic H_2 injection and withdrawal at 5 mL/h (Exp B3), with the combined images of S_{gi} (blue + purple) and S_{gr} (red + purple). In general, the H_2 distribution varied between the cycles but was similar between cycles 2 and 3. The S_{gi} tended to distribute in the large, connected pore clusters (middle right area of the images), whereas the S_{gr} distribution changed over the cycles showing hysteresis despite having similar S_{gr} values of ~0.30. (For interpretation of the references to color in this figure legend, the reader is referred to the Web version of this article.)

mechanisms were independent of pressure in the 5–40 bar range.

Cyclic injections resulted in fluctuating H_2 saturation between 0.42 and 0.67 after drainage, due to the H_2 movement from outside the FoV (Fig. 3, Exp B3). H_2 preferentially occupied the large, connected pore clusters (middle, right region of the images in Fig. 3). The residual H_2 saturation after imbibition exhibited little variation over several cycles (average

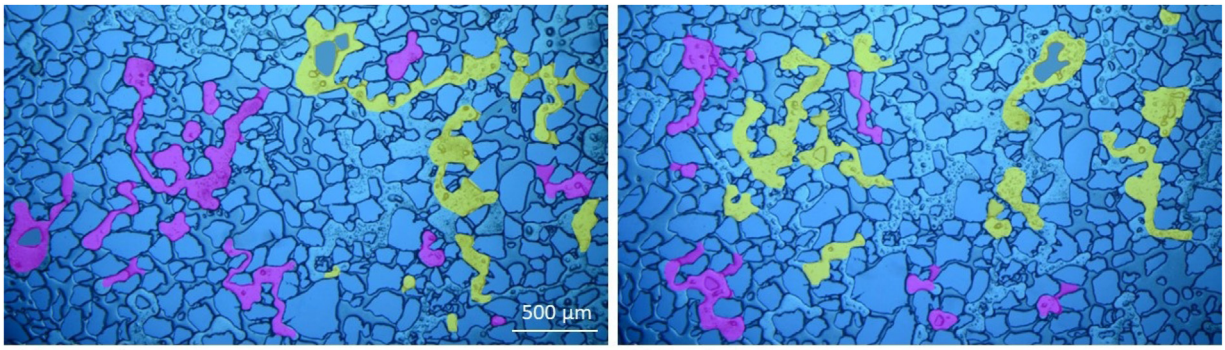

Fig. 4 – H_2 reconnection with the injected H_2 in the subsequent drainage cycle: (a) From cycle 3 to 4 at 2.5 mL/h (3 → 4), and (b) from cycle 4 to 5 at 5 mL/h (4 → 5). H_2 reconnection seemed somewhat stochastic locally but was favored in the large pore clusters with wide pore throats. A portion of the disconnected H_2 after imbibition, S_{gr} (dis) (yellow + purple) connected with the injected H_2 during the subsequent drainage (yellow) and the rest remained as disconnected, S_{gi} (dis) (purple). The injected H_2 is not manually segmented and appears in the image in its original light blue color. (For interpretation of the references to color in this figure legend, the reader is referred to the Web version of this article.)

$S_{gr} = 0.31 \pm 0.03$), however, its pore space distribution varied between cycles due to hysteresis. Variations in the residual H_2 distribution have also been reported during core flooding and μCT imaging, despite equal residual H_2 saturations [30]. In our case, the residually trapped H_2 was not necessarily immobile in the subsequent cycle and could reconnect with the injected H_2, described next.

The ability of H_2 ganglia to reconnect seemed stochastic locally between pores but the global distribution appeared to depend on the pore cluster morphology (Fig. 4). The H_2 ganglia in proximity to pore clusters with wide pore throats tended to reconnect during drainage (yellow in Fig. 4), whereas H_2 ganglia remained disconnected in the pores with narrow pore throats (purple in Fig. 4). In contrast, the core flooding experiments with μCT imaging showed that the residual CO_2 ganglia size gradually changed with increasing number of cycles, penetrating smaller pore throats [32,33]. Reconnection of H_2 ganglia during drainage was in general high, characterized by the amount reduction of H_2 ganglia in 9 out of 12 drainage injections relative to previous imbibition injections (Fig. 5). High H_2 ability to reconnect is favorable for real storage projects, reducing H_2 loss during cyclic injections.

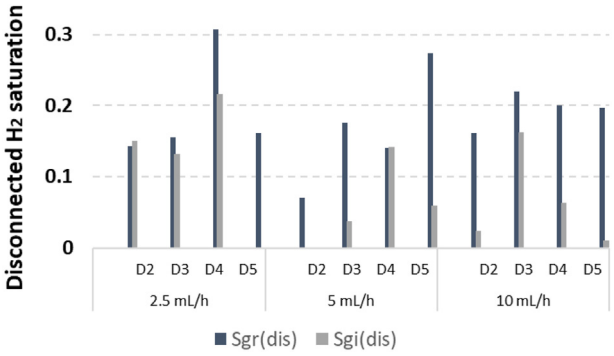

Fig. 5 – Quantification of the H_2 ganglia reconnection, by comparing the disconnected H_2 saturation after imbibition, S_{gr} (dis) (blue) and the subsequent drainage cycle, S_{gi} (dis) (gray) at the injection rates of 2.5, 5 and 10 mL/h. The horizontal axis compares the two subsequent cycles: The transition from the imbibition cycle 1 to the drainage cycle 2 is denoted as D2. In most cases, the disconnected H_2 saturation decreased in the subsequent drainage cycle, indicating high reconnection ability. (For interpretation of the references to color in this figure legend, the reader is referred to the Web version of this article.)

Microscopic storage capacity

Microscopic H_2 storage capacity was evaluated based on capillary number correlation (CNC) and pore pressures (Fig. 6, Table 3). The initial H_2 saturation after drainage changed both monotonically (at 5 bar) and nonmonotonically (at 1, 30 and 40 bar) with increased capillary number. A monotonic increase after a plateau region was consistent with classic CNC at core scale [44] and some microfluidic studies [41,45]. Nonmonotonic trends were also reported from micromodels [46–48], likely due to the crossover from capillary to viscous flow regimes and/or micromodel properties [44].

When averaged for a specific capillary number, the initial H_2 saturation exhibited a monotonic trend (Fig. 6). The critical drainage capillary number ranged between $3.4–6.8 \times 10^{-7}$, corresponding to maximum H_2 storage capacity of ~60% of the pore space. The optimal reservoir scale injection rate yielding the highest storage capacity would therefore be in the range of ~170–340 thousand standard m^3/day, assuming the injector perforation length of 30 m and the experimental injection velocity. Our storage capacity and injection rates were comparable with the reservoir simulations of aquifer storage assuming maximum H_2 saturations of 70% and injection rates of ~200–300 thousand standard m^3/day [11,12,49].

No clear pressure effect was observed on the initial H_2 saturation, contradicting classic threshold pressure phenomena [50]. The saturation independence from pressure was likely due to insignificant wettability and interfacial tension alterations in the H_2–H_2O systems under the studied pressure range of 1–40 bar. The H_2 contact angles (i.e. wettability)

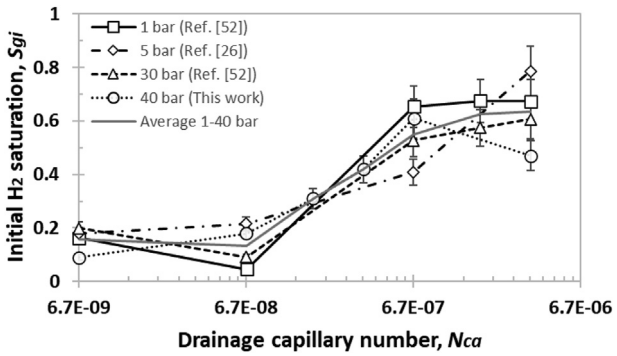

Fig. 6 – Microscopic H_2 storage capacity from the capillary number correlation (CNC) compared with the results from the same micromodel at 1, 5, and 30 bar [26,52]. The S_{gi} was independent of pressure. The maximum H_2 storage capacity was on average equal to ~60% of the pore space (gray curve). The error bars represent the image analysis relative uncertainty (9%).

showed no pressure dependence under the range of 20–100 bar in Berea and Bentheimer sandstones [14]. Insignificant contact angle changes of ~5° were reported for H_2 on the pure quartz surface for pore pressures ranging between 1 and 50 bar and room temperature [16]. The H_2–H_2O interfacial tension increases by less than 1% from 1 to 40 bar [38]. No correlation between initial gas saturation and pressure has been reported for CO_2, N_2, and H_2 at core scale [30,51], corroborating our results.

Residual trapping and microscopic recovery during cyclic injections

The initial and residual H_2 saturations were quantified for cyclic injections and the corresponding microscopic recovery factor was calculated for every cycle (Fig. 7, Table 3). The H_2 saturation range between the cycles depended on the injection rate, in accordance with the critical capillary number from the CNC (Fig. 6). The low injection rate (1 mL/h) resulted in a low saturation range between 0.03 and 0.14 (Fig. 7a), with an increase up to 0.27–0.73 at higher injection rates (≥2.5 mL/h) (Fig. 7b–d). The initial H_2 saturation varied between the cycles at higher injection rates, whereas the residual H_2 remained nearly constant and equal to ~0.43 at 2.5 mL/h, ~0.31 at 5 mL/h, and ~0.29 at 10 mL/h, explained next.

The reason for the fluctuations in the initial H_2 saturation could be twofold: 1) H_2 redistribution from outside the FoV, caused by random H_2 injection patterns, and/or 2) the presence of the disconnected H_2 ganglia. A further analysis (Fig. 8) revealed that both connected and disconnected H_2 saturation were stochastic without any clear trend, meaning that H_2 redistribution (reason 1) was the main cause for the fluctuating initial saturations. The opposite was observed for *n*-hexane (C_6H_{14}, used as a proxy for CO_2) cyclic injections in a micromodel, where the amount of the disconnected C_6H_{14} increased over the cycles due to the converged injection patterns through the most accessed pore channels [53]. The discrepancies with our study were likely caused by the differences in the micromodel design. In our case, two open

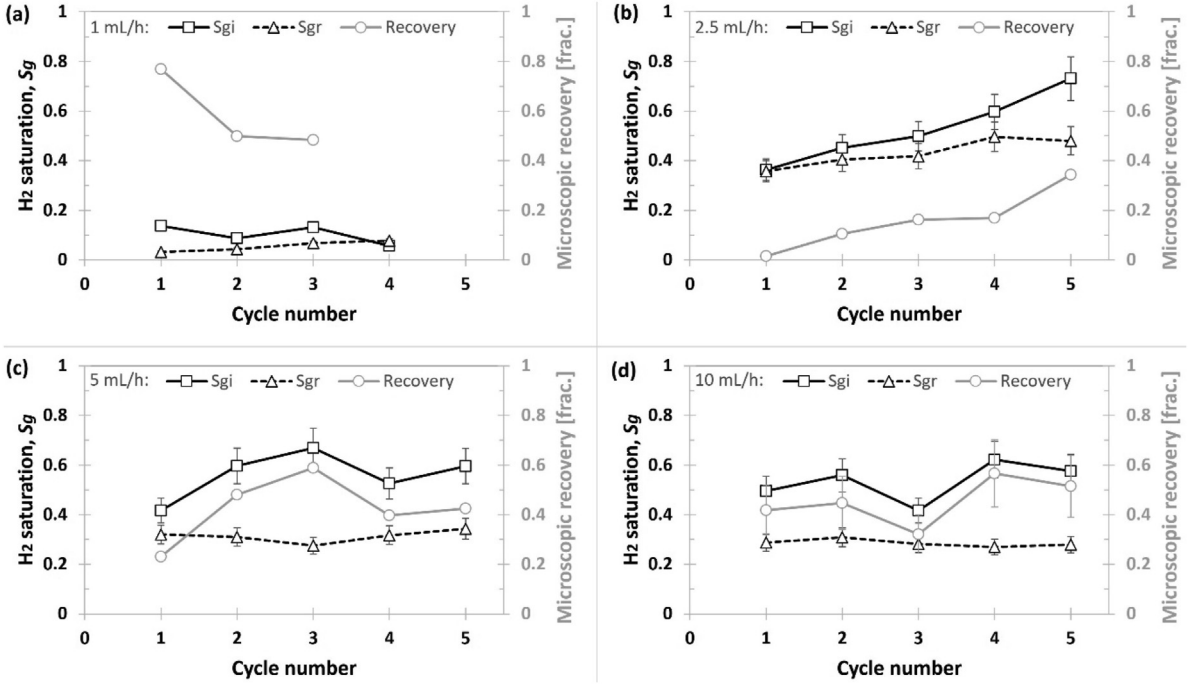

Fig. 7 – Initial (S_{gi}) and residual (S_{gr}) H_2 saturation and the resulting microscopic recovery factors during cyclic injections at the flow rate of: (a) 1 mL/h, (b) 2.5 mL/h, (c) 5 mL/h, (d) 10 mL/h. The S_{gi} fluctuated between the cycles due to H_2 redistribution from outside the FoV. In contrast, the S_{gr} showed better reproducibility, with nearly constant values throughout the cycles. The microscopic recovery factors reflected the fluctuations in the S_{gi}. The error bars represent the image analysis relative uncertainty (9%).

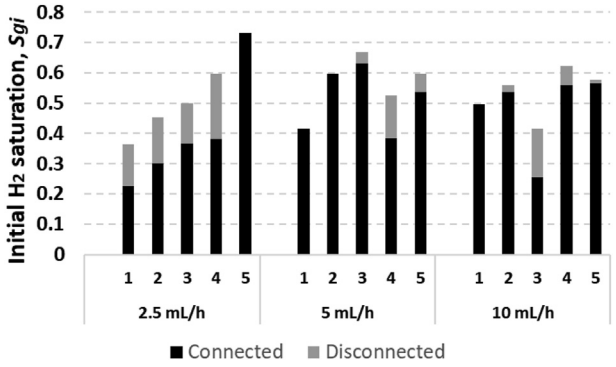

Fig. 8 – Share of the connected and disconnected initial H_2 saturation (S_{gi}) during cyclic injections (cycles 1–5) at the injection rate of 2.5, 5 and 10 mL/h. No clear trend was observed, meaning that the presence of the disconnected H_2 did not cause the fluctuations in the S_{gi} in Fig. 7.

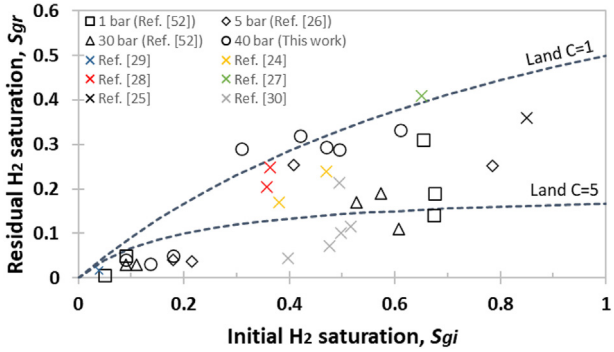

Fig. 9 – Trapping model based on H_2 saturations after primary drainage (S_{gi}) and imbibition (S_{gr}), combined with the results from the same micromodel at 1, 5 and 30 bar [26,52] and the literature H_2 data at core scale denoted by colored crosses [24,25,27–30]. Most of the measurements followed the Land trapping model with the trapping coefficients C = 1 and C = 5. The upper limit data points were comparable to CO_2 with the trapping coefficients between 0.2 and 2.1 in sandstones [56,57].

channels along the micromodel length (Fig. 1) resulted in crossflow, facilitating more random injection patterns in multiple directions. In the case of C_6H_{14} injections, the open channels were built in the opposite direction, that is along the micromodel widths, creating one-directional injection pattern.

Contrary to the initial H_2 saturation, the residual H_2 saturation was more reproducible because the H_2O injection was eased in a strongly hydrophilic system, with well-established injection patterns through the wetting H_2O films coating the grain surfaces. Note that natural reservoirs contain organic-rich material, making their rock surfaces more hydrophobic than our micromodel [13,16]. Greater reproducibility of the residual H_2 saturation throughout the cycles is beneficial from the storage perspective, permitting a better control of the H_2 loss due to residual trapping. The distribution of the residual H_2, however, visually changed over the cycles as mentioned in section 3.1 (Fig. 3). Such hysteretic behavior due to residual trapping can affect the imbibition relative permeability, and hysteresis in H_2–H_2O relative permeability has already been demonstrated at core scale [24,25].

The microscopic recovery factors, defined as $(S_{gi} - S_{gr})/S_{gi}$, fluctuated between the cycles, in alignment with the initial H_2 saturation (Fig. 7). The recovery factors ranged between 2% and 77% with an average of ~40%, comparable with the recovery factors from reservoir simulations of H_2 storage in the H_2O zone of a depleted hydrocarbon field: 49% [54] and aquifer storage: 36–59% [11,55]. Note that recovery factors from reservoir simulations are macroscopic and valid for the entire reservoir, contrary to microfluidics which deal with the microscopic phenomena. The highest H_2 saturation is expected in the near-well area, with gradually decreasing H_2 saturation when approaching the H_2–H_2O transition zone in the far-well area [11,12,49]. During cyclic injections, the H_2–H_2O transition boundary is constantly moving, resulting in increasing H_2O saturation during H_2 withdrawal with associated residual H_2 trapping. Hence, the reported microscopic recovery factors are mostly relevant for the H_2–H_2O transition zone.

Trapping model

We combine H_2 saturations after primary drainage and imbibition together with the results from the same micromodel at 1–30 bar and available H_2 data at core scale (Fig. 9), to construct H_2 trapping relationship based on an empirical Land model [34]. This model was derived from the measurements of the initial and residual gas saturations in sandstone core samples, defined as follows: $S_{gr} = S_{gi}/(1 + C{\cdot}S_{gi})$, where C is the trapping coefficient. The data points were greatly scattered and mostly fell within the trapping coefficient (C) range between 1 and 5. The upper boundary points matched the CO_2 trapping models in different sandstones, with the trapping coefficient range of 0.2–2.1 [56,57]. In contrast, the lower boundary points were outside the reported CO_2 data, indicating that less H_2 trapping may be expected compared to CO_2. The lower boundary points disagreed with the contact angle measurements which reported less H_2 wetting (more hydrophilic) compared to CO_2 [13,16], that in turn implies more H_2 trapping [23]. Greater scatter and disagreement of lower boundary H_2 data points with CO_2 data could be due to the differences in the porous materials and methodologies. The CO_2 measurements were obtained from conventional core flooding with the core length of 6–12 cm, whereas microfluidics and shorter core plugs of 1.5–5.7 cm were used for most H_2 saturation measurements.

The initial and residual H_2 saturations from cyclic injections (Fig. 10) showed no significant increase in residual trapping over the cycles for similar initial H_2 saturations, consistent with the Land model and corroborated by H_2 [30] and some CO_2 cyclic injection studies [58,59]. In contrast, some CO_2 measurements deviated from the Land model, with a sharp increase in residual saturations over the injection cycles [31–33]. The exact mechanism for this deviation is still poorly understood but could be attributed to pore throat blockage due to fines migration, CO_2 adhesion to the grain surfaces, and/or wettability alteration to a "patchy" mixed-

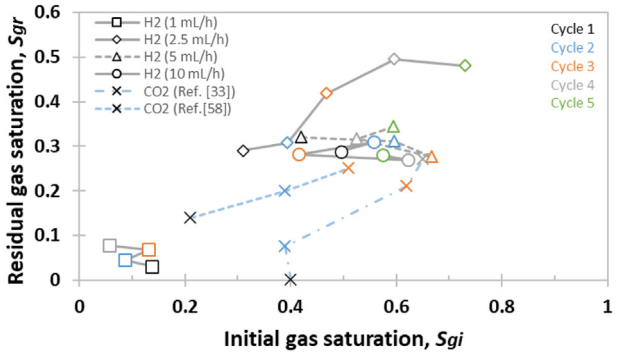

Fig. 10 – Initial (S_{gi}) and residual (S_{gr}) H_2 saturations during cyclic injections at the injection rates of 1, 2.5, 5 and 10 mL/h. The S_{gr} were nearly stable over the injection cycles for similar S_{gi}, consistent with the Land trapping model. Our results were compared with CO_2 studies (denoted by crosses), where there is currently a contradiction, with some studies following the Land model [58] and other studies deviating from it [33].

wet with discontinuous CO_2-wet areas [33,60]. Even though our results and one core scale H_2 study [30] did not indicate a significant increase in residual trapping, lack of H_2 studies and the disagreement in the CO_2 literature emphasizes the importance for further investigations of H_2 cyclic injections. A potential increase in residual H_2 trapping over the injection cycles is undesired as it will reduce H_2 storage efficiency.

Trapping models based on the 2D microfluidic experiments have a limited applicability for 3D reservoirs due to the small volume and the absence of gravity and heterogeneity. The same applies for the storage capacities and recovery factors quantified in sections 3.2 and 3.3. The 2D micromodels are suitable for qualitative description of the pore scale flow mechanisms, which can support core scale measurements. Extrapolation of the quantitative results to natural reservoirs requires caution and should be preferably done by pore scale modelling. However, our results followed classic CNC trends (Fig. 6) and the H_2 saturations were within the literature range at core scale (Fig. 9). Therefore, it is reasonable to claim that the quantified H_2 storage capacities and trapping model from microfluidics can temporarily substitute for missing measurements until a comprehensive core scale dataset is available.

Conclusions

We report a series of cyclic H_2– H_2O injections in a micromodel mimicking sandstone pore patterns and relevant for shallow H_2 storage in aquifers and depleted gas fields with an underlying water zone. We found that H_2 saturation after primary drainage increased with increasing capillary number, with maximum storage capacities up to ~60% of the pore scape. When combined with previous results from the same micromodel, the initial H_2 saturation was independent of pressure in the range of 1–40 bar. The distribution of initial and residual H_2 in the pore space were hysteretic over the injection cycles, with fluctuating initial but similar residual H_2 saturations. The residually trapped H_2 showed good reconnection ability, which was favored in proximity to the large pore clusters with wide pore throats. The H_2 trapping followed the Land model, with trapping coefficient between 1 and 5 where the upper limit values matched the CO_2 trapping models in sandstones. The microscopic H_2 recovery factors varied due to the fluctuating initial H_2 saturation and on average were equal to ~40%, relevant for the H_2–H_2O transition zone in the far-well area. Higher reconnection ability and reproducibility of residual H_2 saturation are beneficial for underground H_2 storage but this positive impact may be suppressed by its hysteretic distribution over the injection cycles. Future work should be focused on core scale cyclic injections and on pore scale modelling for upscaling to natural reservoirs.

Declaration of Competing Interest

The authors declare that they have no known competing financial interests or personal relationships that could have appeared to influence the work reported in this paper.

Acknowledgements

The authors gratefully acknowledge the financial support from the University of Bergen and from the Research Council of Norway under projects *Hydrogen Storage in Subsurface Porous Media—Enabling Transition to Net-Zero Society* (project number 325457) and Centre for Sustainable Subsurface Resources (project number 331841).

REFERENCES

[1] Navaid HB, Emadi H, Watson M. A comprehensive literature review on the challenges associated with underground hydrogen storage. Int J Hydrogen Energy 2023;48(28):10603–35.
[2] Undertaking HJ. Hydrogen roadmap Europe: a sustainable pathway for the European energy transition. 2019.
[3] Cihlar J, Mavins D, van der Leun K. Picturing the value of underground gas storage to the European hydrogen system. Guidehouse; 2021.
[4] Carden PO, Paterson L. Physical, chemical and energy aspects of underground hydrogen storage. Int J Hydrogen Energy 1979;4(6):559–69.
[5] Muhammed NS, et al. A review on underground hydrogen storage: insight into geological sites, influencing factors and future outlook. Energy Rep 2022;8:461–99.
[6] Pérez A, et al. Patagonia wind - hydrogen project: underground storage and methanation. In: 21st world hydrogen energy conference. Spain: Zaragoza; 2016.
[7] RAG, *RAG Austria AG - Underground Sun Storage*. Final report public13; 2020.
[8] Panfilov M. Underground and pipeline hydrogen storage. In: Compendium of hydrogen energy. Woodhead Publishing; 2016.
[9] Smigan P, et al. Methanogenic bacteria as a key factor involved in changes of town gas stored in an underground reservoir. FEMS Microbiol Ecol 1990;73(3):221–4.

[10] Dopffel N, Jansen S, Gerritse J. Microbial side effects of underground hydrogen storage - knowledge gaps, risks and opportunities for successful implementation. Int J Hydrogen Energy 2021;46(12):8594–606.
[11] Lubon K, Tarkowski R. Numerical simulation of hydrogen injection and withdrawal to and from a deep aquifer in NW Poland. Int J Hydrogen Energy 2020;45(3):2068–83.
[12] Sainz-Garcia A, et al. Assessment of feasible strategies for seasonal underground hydrogen storage in a saline aquifer. Int J Hydrogen Energy 2017;42(26):16657–66.
[13] Ali M, et al. Hydrogen wettability of quartz substrates exposed to organic acids; Implications for hydrogen geo-storage in sandstone reservoirs. J Petrol Sci Eng 2021;207.
[14] Hashemi L, et al. Contact angle measurement for hydrogen/brine/sandstone system using captive-bubble method relevant for underground hydrogen storage. Adv Water Resour 2021;154.
[15] Higgs S, et al. In-situ hydrogen wettability characterisation for underground hydrogen storage. Int J Hydrogen Energy 2022;47(26):13062–75.
[16] Iglauer S, Ali M, Keshavarz A. Hydrogen wettability of sandstone reservoirs: implications for hydrogen geo-storage. Geophys Res Lett 2021;48(3).
[17] Hashemi L, et al. A comparative study for H2–CH4 mixture wettability in sandstone porous rocks relevant to underground hydrogen storage. Adv Water Resour 2022;163.
[18] van Rooijen W, et al. Microfluidics-based analysis of dynamic contact angles relevant for underground hydrogen storage. Adv Water Resour 2022;164.
[19] Al-Yaseri A, Jha NK. On hydrogen wettability of basaltic rock. J Petrol Sci Eng 2021;200.
[20] Pan B, Yin X, Iglauer S. Rock-fluid interfacial tension at subsurface conditions: implications for H2, CO2 and natural gas geo-storage. Int J Hydrogen Energy 2021;46(50):25578–85.
[21] Pan B, et al. Underground hydrogen storage: influencing parameters and future outlook. Adv Colloid Interface Sci 2021:294.
[22] Raza A, et al. A holistic overview of underground hydrogen storage: influencing factors, current understanding, and outlook. Fuel 2022:330.
[23] Iglauer S, Pentland CH, Busch A. CO2 wettability of seal and reservoir rocks and the implications for carbon geo-sequestration. Water Resour Res 2015;51(1):729–74.
[24] Boon M, Hajibeygi H. Experimental characterization of H-2/water multiphase flow in heterogeneous sandstone rock at the core scale relevant for underground hydrogen storage (UHS). Sci Rep 2022;12(1).
[25] Lysyy M, et al. Hydrogen relative permeability hysteresis in underground storage. Geophys Res Lett 2022;49(17).
[26] Lysyy M, Ersland G, Ferno M. Pore-scale dynamics for underground porous media hydrogen storage. Adv Water Resour 2022;163.
[27] Jha NK, et al. Pore scale investigation of hydrogen injection in sandstone via X-ray micro-tomography. Int J Hydrogen Energy 2021;46(70):34822–9.
[28] Jangda Z, et al. Pore-scale visualization of hydrogen storage in a sandstone at subsurface pressure and temperature conditions: trapping, dissolution and wettability. J Colloid Interface Sci 2023;629:316–25.
[29] Al-Yaseri A, et al. Initial and residual trapping of hydrogen and nitrogen in Fontainebleau sandstone using nuclear magnetic resonance core flooding. Int J Hydrogen Energy 2022;47(53):22482–94.
[30] Thaysen, Eike M, et al. Pore-scale imaging of hydrogen displacement and trapping in porous media. Int J Hydrogen Energy 2023;48(8):3091–106.
[31] Edlmann K, et al. Cyclic CO2 - H2O injection and residual trapping: implications for CO2 injection efficiency and storage security. Int J Greenh Gas Control 2019;80:1–9.
[32] Herring AL, Andersson L, Wildenschild D. Enhancing residual trapping of supercritical CO2 via cyclic injections. Geophys Res Lett 2016;43(18):9677–85.
[33] Herring AL, et al. Evolution of bentheimer sandstone wettability during cyclic scCO(2)-brine injections. Water Resour Res 2021;57(11).
[34] Land CS. Calculation of imbibition relative permeability for two and three-phase flow from rock properties. Soc Petrol Eng J 1968;8(2):149–&.
[35] Benali B, et al. Pore-scale bubble population dynamics of CO2-foam at reservoir pressure. Int J Greenh Gas Control 2022;114.
[36] Buchgraber M, et al. Creation of a dual-porosity micromodel for pore-level visualization of multiphase flow. J Petrol Sci Eng 2012;86–87:27–38.
[37] Linstrom PJ, Mallard WG. The NIST Chemistry WebBook: a chemical data resource on the internet. J Chem Eng Data 2001;46(5):1059–63.
[38] Chow YTF, Maitland GC, Trusler JPM. Interfacial tensions of (H2O + H2) and (H2O + CO2 + H2) systems at temperatures of (298–448) K and pressures up to 45 MPa. Fluid Phase Equil 2018;475:37–44.
[39] Chomsurin C, Werth CJ. Analysis of pore-scale nonaqueous phase liquid dissolution in etched silicon pore networks. Water Resour Res 2003;39(9).
[40] Zhao X, Jin H. Investigation of hydrogen diffusion in supercritical water: a molecular dynamics simulation study. Int J Heat Mass Tran 2019;133:718–28.
[41] Zhang CY, et al. Influence of viscous and capillary forces on immiscible fluid displacement: pore-scale experimental study in a water-wet micromodel demonstrating viscous and capillary fingering. Energy Fuels 2011;25(8):3493–505.
[42] Roof JG. Snap-off of oil droplets in water-wet pores. Soc Petrol Eng J 1970;10(1):85. &.
[43] Lenormand R, Zarcone C, Sarr A. Mechanisms of the displacement of one fluid by another in a network of capillary ducts. J Fluid Mech 1983;135(Oct):337–53.
[44] Guo H, Song KP, Hilfer R. A brief review of capillary number and its use in capillary desaturation curves. Transport Porous Media 2022;144(1):3–31.
[45] Chang C, et al. Scaling the impacts of pore-scale characteristics on unstable supercritical CO2-water drainage using a complete capillary number. Int J Greenh Gas Control 2019;86:11–21.
[46] An SY, et al. Transition from viscous fingering to capillary fingering: application of GPU-based fully implicit dynamic pore network modeling. Water Resour Res 2020;56(12).
[47] Chang C, et al. Impacts of mixed-wettability on brine drainage and supercritical CO2 storage efficiency in a 2.5-D heterogeneous micromodel. Water Resour Res 2020;56(7).
[48] de Castro AR, et al. Experimental study on nonmonotonicity of Capillary Desaturation Curves in a 2-D pore network. Water Resour Res 2015;51(10):8517–28.
[49] Bai T, Tahmasebi P. Coupled hydro-mechanical analysis of seasonal underground hydrogen storage in a saline aquifer. J Energy Storage 2022;50.
[50] Thomas LK, Katz DL, Tek MR. Threshold pressure phenomena in porous media. Soc Petrol Eng J 1968;8(2):174. &.
[51] Niu B, Al-Menhali A, Krevor SC. The impact of reservoir conditions on the residual trapping of carbon dioxide in Berea sandstone. Water Resour Res 2015;51(4):2009–29.
[52] van der Hart PHK. A pore-scale study of underground hydrogen storage in porous media. The University of Bergen; 2021.

[53] Ahn H, et al. Migration and residual trapping of immiscible fluids during cyclic injection: pore-scale observation and quantitative analysis. Geofluids; 2020. p. 2020.
[54] Lysyy M, Ferno M, Ersland G. Seasonal hydrogen storage in a depleted oil and gas field. Int J Hydrogen Energy 2021;46(49):25160–74.
[55] Mahdi DS, et al. Hydrogen underground storage efficiency in a heterogeneous sandstone reservoir. Advances in Geo-Energy Research 2021;5(4):437–43.
[56] Krevor SCM, et al. Relative permeability and trapping of CO2 and water in sandstone rocks at reservoir conditions, vol.48. Water Resources Research; 2012.
[57] Ni H, et al. Predicting CO2 residual trapping ability based on experimental petrophysical properties for different sandstone types. Int J Greenh Gas Control 2019;86:158–76.
[58] Ruprecht C, et al. Hysteretic trapping and relative permeability of CO2 in sandstone at reservoir conditions. Int J Greenh Gas Control 2014;27:15–27.
[59] Saeedi A, et al. Multiphase flow behaviour during CO2 geo-sequestration: emphasis on the effect of cyclic CO2-brine flooding. J Petrol Sci Eng 2011;79(3–4):65–85.
[60] Ge JC, Zhang XZ, Le-Hussain F. Fines migration and mineral reactions as a mechanism for CO2 residual trapping during CO2 sequestration. Energy 2022:239.